Electronic Supplementary Material (ESI) for Journal of Materials Chemistry A.

Electronic supplementary Information for:

Bichannel Design Inspired by Membrane Pump: A Rate Booster for Conversion-type Anode of Sodium Ion Battery†

Bo Yin,‡[a] Haiyong He,‡*[a] Jiande Lin,[b] Youran Hong,[c] Boshi Cheng,[a] Lin Zhu,[a] Hualong He,[a] Mingchan Ma[a] and Jiangwei Wang[c]

[a] Ningbo Institute of Materials Technology and Engineering, Chinese Academy of Sciences Ningbo 315201, P.R. China, E-mail: hehaiyong@nimte.ac.cn

[b] State Key Laboratory of Physical Chemistry of Solid Surfaces, College of Chemistry and Chemical Engineering, Xiamen University, Xiamen 361005, P.R. China

[c] Center of Electron Microscopy and State Key Laboratory of Silicon Materials, School of Materials Science and Engineering, Zhejiang University, Hangzhou 310027, P.R. China

‡ These authors contributed equally to this work.

* Corresponding authors

† Electronic supplementary information (ESI) available. See DOI:10.1039/xxxxx.

Experimental section

Synthesis of $Co_2P_2O_7/C$ (CPOC) and $Co_2P_2O_7/C@C$ (CPOC@C): The Co(II)-ATMP complexes was first synthetized, then coated by dopamine and finally annealed to obtain CPOC@C. In a typical experiment, 3 mmol cobaltous acetate tetrahydrate and 1 mmol amino trimethylene phosphonic acid (ATMP, 50% aqueous solution) were dispersed in 20 mL dimethyl formamide (DMF) separately. The ATMP solution was then added into Co^{2+} contained solution dropwise, and intensively stirred at room temperature for 8 h. In the following step, 5 mL 0.2 mM DMF solution of dopamine hydrochloride was added and the stirred continuously for another 12 h. The Co(II)-ATMP @dopamine was separated by vacuum filtration and purified by DMF three times. After vacuum drying at 80 °C for 12 h, the as-prepaed ash black product was calcined at 600, 700 and 800 °C for 2 h with the ramp of 2 °C/ min in a tube furnace under Ar atmosphere. The final products, namely $Co_2P_2O_7/C@C$-600, $Co_2P_2O_7/C@C$-700, $Co_2P_2O_7/C@C$-800, were marked as CPOC@C-600, CPOC@C-700 and CPOC@C-800, respectively. The fabrication of $Co_2P_2O_7/C$ (denoted as CPOC) was the same as CPOC@C-700 except for the absence of dopamine hydrochloride solution.

Synthesis of $Co_2P_2O_7$ (CPO): Preparation of $Co_2P_2O_7$ from inorganic pyrophosphate was based on the method proposed by Yuan et.al.[1] Firstly, $Na_2H_2P_2O_7$ was obtained by annealing NaH_2PO_4 at 210 °C for 16 h in a muffle furnace, then 1.8 g of $Na_2H_2P_2O_7$ and 2 g of CH_3COONH_4 were dissolved in 45 mL deionized water. After that, 7.5 mL of 0.33 M $Co(CH_3COO)_2·4H_2O$ aqueous solution was slowly dropped into the above solution. Following the 8 h continuous stirring, a light purple precursor was separated from the mother liquor and dried in an oven. Finally, the obtained precursor was subjected to the same heat treatment as CPOC to obtain $Co_2P_2O_7$ (denoted as CPO).

Synthesis of $M_2P_2O_7/C@C$ (M=Mn, Fe, Zn): Preparation of M(II)-ATMP (M=Mn, Fe, Zn) complexes were similar to Co(II)-ATMP, while the cobaltous acetate was replaced by manganese acetate, ferric acetate and zinc acetate, respectively. The obtained precursors were then annealed at appropriate temperatures, and the calcined products were marked as MPOC@C-XXX (XXX stands for the annealing temperature).

Materials characterizations:

Cold filed emission scanning electron microscopy (Hitachi, S4800) and transmission electron microscopy (FEI, Tecnai F20) were used jointly to obtain detailed microstructural information of the prepared samples. Thermogravimetric/Differemtial Thermal Analyzer (Pyris Diamond TG/DTA, Perkin-Elmer) was used to analyze the mass change during thermal treatment and identify phase transition temperature. X-ray diffraction patterns were recorded on a Bruker D8 Advance Davinci with Cu radiation. Raman spectra were acquired on a Renishaw inVia Reflex with a 532 nm laser. Fourier transform infrared spectroscopy were obtained with a Thermo Nicolet 6700. X-ray photoelectron spectroscopy were collected by Shimadzu Axis Ultra DLD. Nitrogen isothermal adsorption and desorption were carried on a Micromeritics ASAP 2020M.

Electrochemical measurements:

The as-prepared active materials were firstly mixed with Super P and CMC at the mass ratio of 8:1:1 to form a uniform slurry, and then coated on a 9 μm thick copper foil. After drying in vacuum for 12 h, the copper foil was punched into 12 mm discs. The acquired electrodes were assembled into CR 2016 type coin cells with sodium metal as counter electrode and glass fiber (Whatman) as separator in a glovebox (Etelux Lab2000) filled with high purity Argon The electrolyte was a solution of 1.0 M $NaClO_4$ in propylene carbonate (PC) with 5% fluoroethylene carbonate (FEC) additive. Galvanostatic discharge/charge measurements were carried out on a LANHE CT2001A multichannel battery test system in the voltage range of 0.01～3.0 V (vs. Na^+/Na). Cyclic voltammetry (CV) curves were recorded on an electrochemical workstation (CHI 660D). After 5 full discharge-charge cycles, the electrochemical impedance spectra (EIS) of CPOC and CPOC@C were collected on a Solartron 1470E cell test system over the frequency range from 100 KHz to 10 mHz.

$Na_3V_2(PO_4)_3$ (NVP) material and electrode were prepared according to the report of Cao et al.[2] The CPOC@C-700 anode first undergo 5 discharge-charge cycles in half cells to form a stable SEI, and then reassembled with NVP cathode to construct full batteries. The cathode/anode mass ratio was set to3:1. The specific capacity of the full battery between 1.0 and 3.7 V was calculated based on the mass of CPOC@C-700.

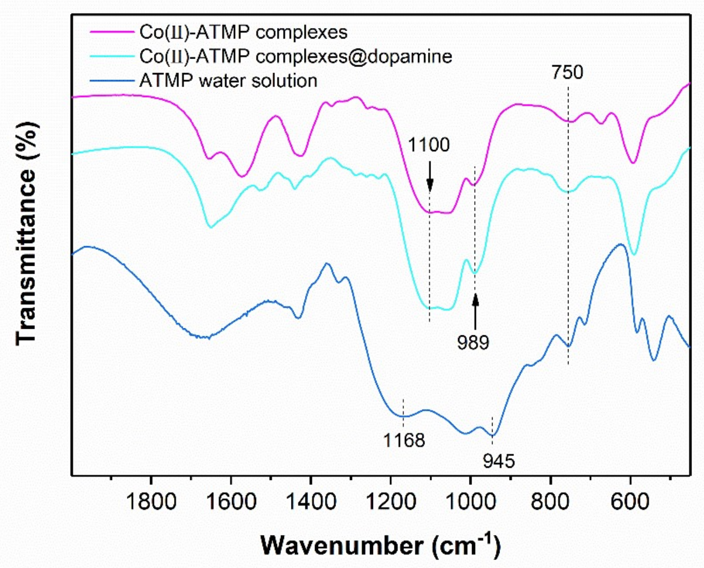

Fig. S1. Fourier transform infrared spectroscopy (FTIR) of ATMP, Co (II)-ATMP complexes and Co (II)-ATMP @dopamine. The bands centered at 750, 945 and 1168 cm^{-1} are assigned to the P-OH, C-N and PO_3 stretching vibration of ATMP. The C-N and PO_3 stretching frequency of the complexes shift to 989 and 1100 cm^{-1}, respectively, suggesting the nitrogen and oxygen atoms of ATMP are coordinated with Co^{2+}.[3]

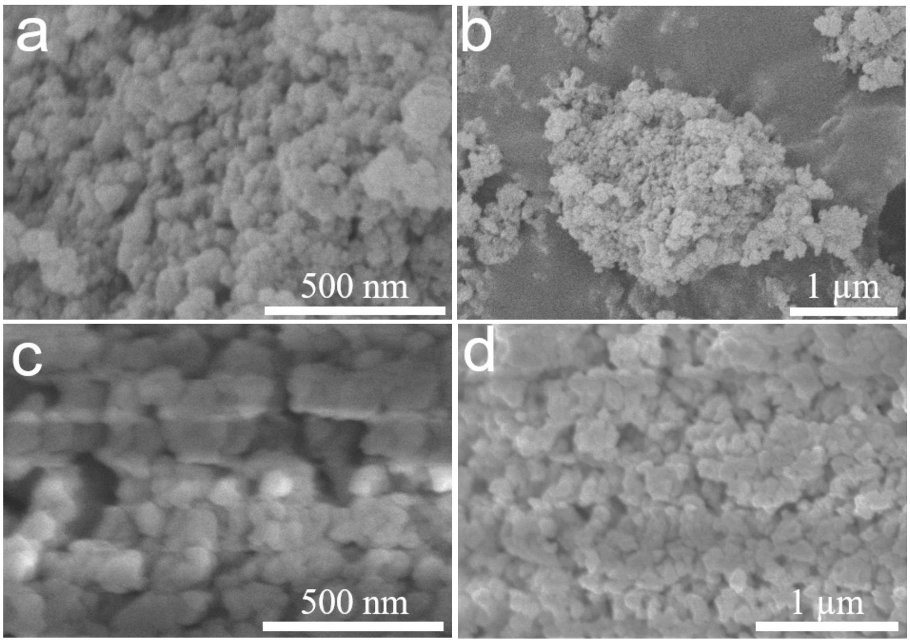

Fig. S2. SEM images of a, b) Co (II)-ATMP complexes and c, d) Co (II)-ATMP @dopamine.

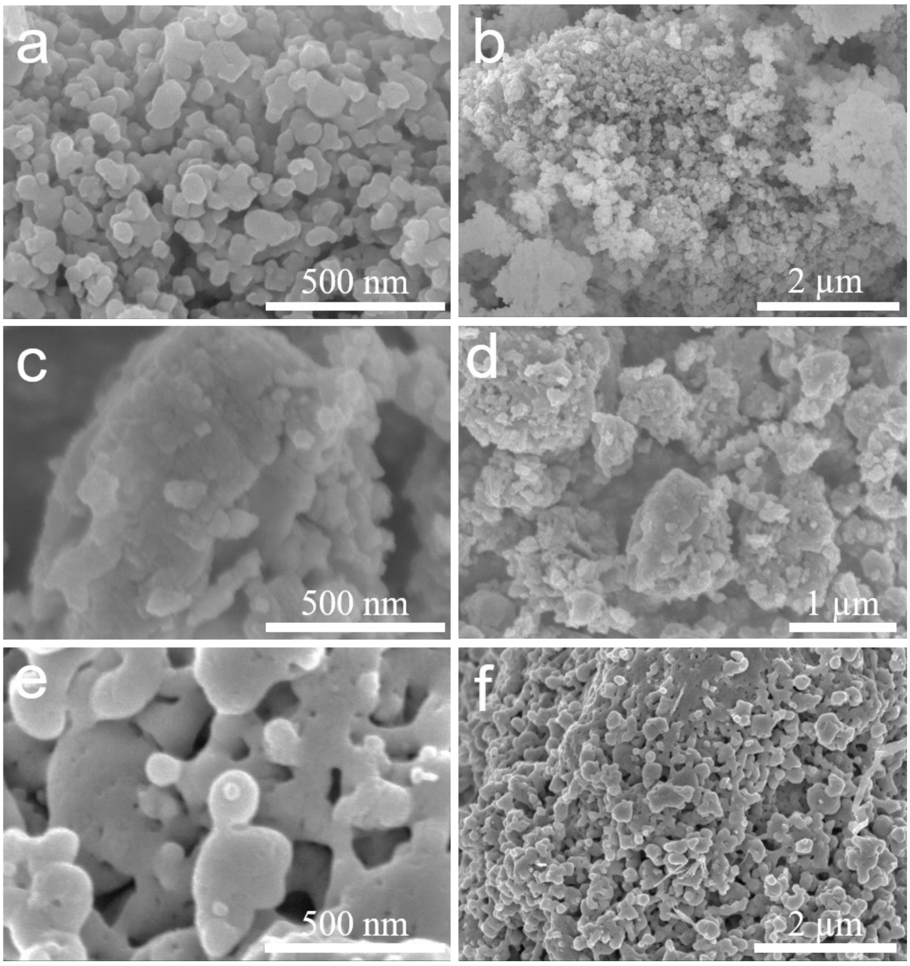

Fig. S3. SEM images of a, b) CPOC@C-600, c, d) CPOC@C-800 and e, f) CPOC.

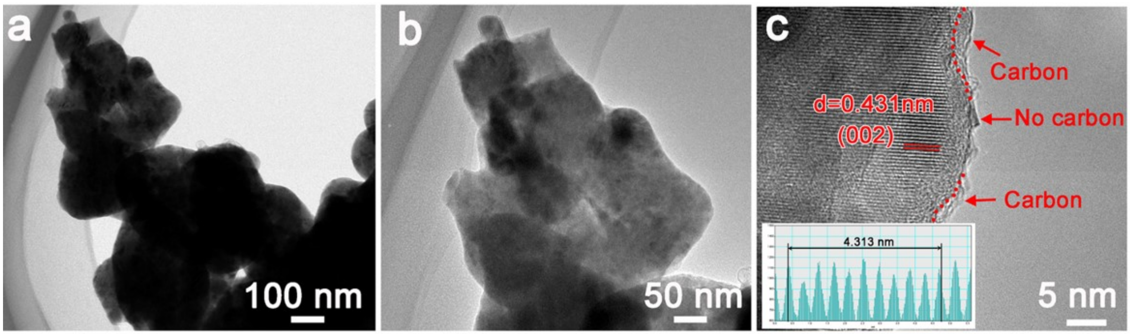

Fig. S4. a, b)TEM and c) HRTEM images of CPOC.

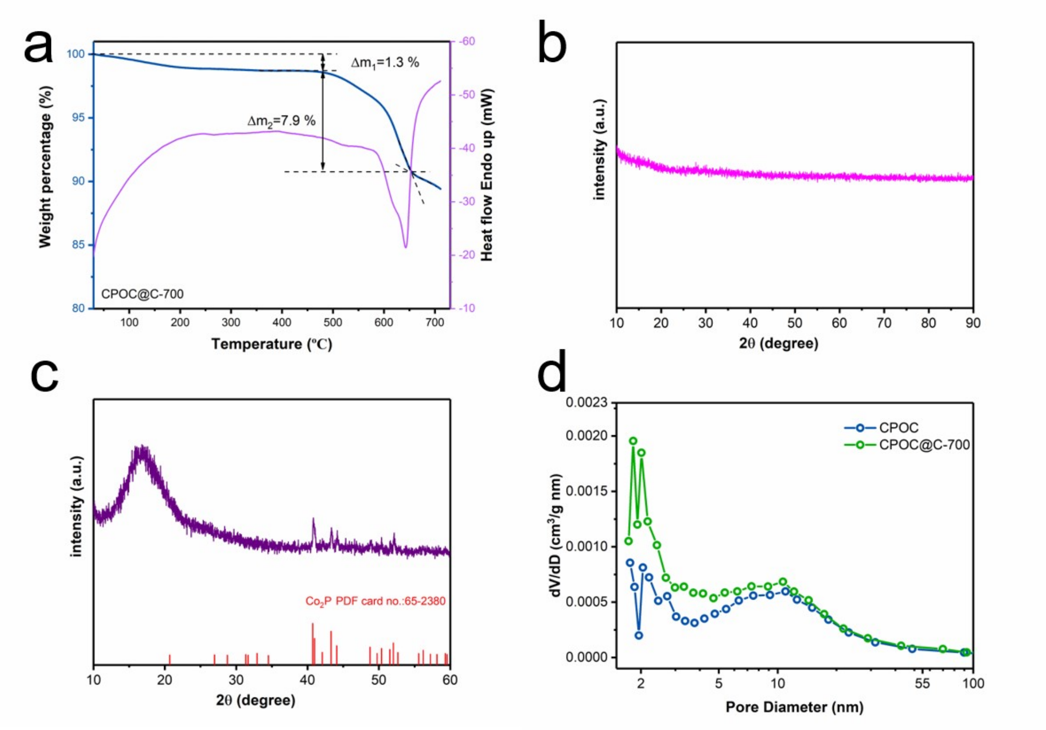

Fig. S5. a) TG and DTA curves of CPOC@C-700. b) XRD of Co (II)-ATMP complexes and c) Co (II)-ATMP @dopamine annealed at 900 °C. d) The pore-size distribution curves of CPOC and CPOC@C-700.

Table S1. Specific surface areas, pore volume analyses of CPOC and CPOC@C-700

Samples	**S_{BET}(m^2/g)**	**V_{pore} (cm^3/g)**	**R_{pore}(nm)**
CPO	8.11	0.022	6.25
CPOC@C-700	10.14	0.023	5.88

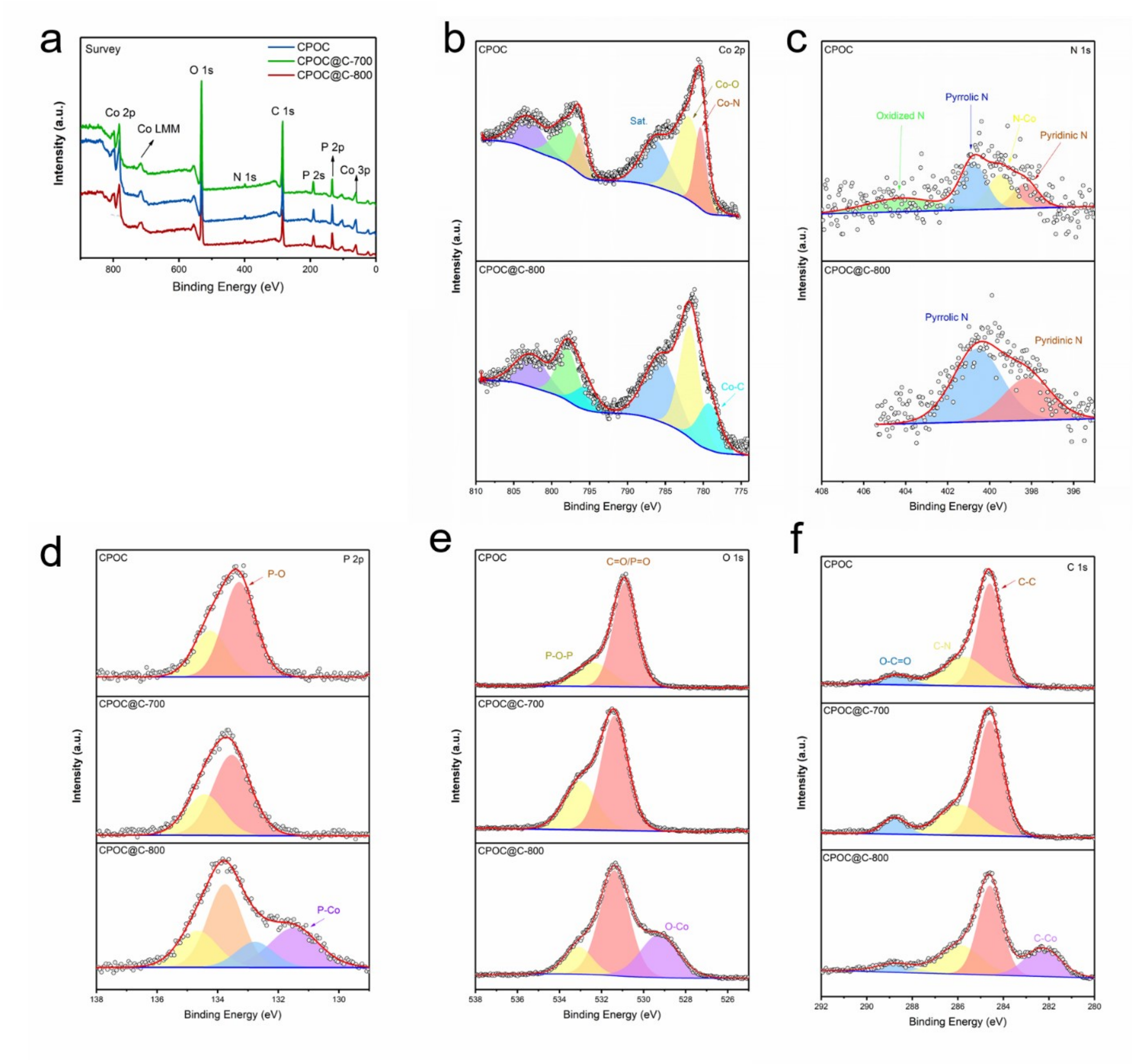

Fig. S6. a) The survey spectra and high-resolution XPS spectra of b) Co 2p, c) N 1s, d) P 2p, e) O 1s and f) C 1s spectra of CPOC and CPOC@Cs.

The survey spectra of CPOC@Cs and CPOC in Fig. S6a confirm the coexistence of Co, P, O, C and N elements, in line with the result of elemental mapping in Fig. 1g. The atomic ratio of Co/P in CPOC@C-700 is 0.92 according to the fitting result of survey spectra, which is close to the proportion of reactants. The high-resolution spectra of each element of CPOC are similar to CPOC@C-700. The two sub-peaks of P 2p at binding energies of 133.5 and 134.4 eV are assigned to P $2p_{3/2}$ and P 2p $_{1/2}$

of PO_4 tetrahedra (Fig. S6d).[4] In the case of O1s spectra, the peaks centered at 531.4 and 533.0 eV can be attributed to C=O/P=O bonding and symmetric oxygen bridging in P-O-P groups, respectively.[5] The C 1s fine spectra in Fig. S6f indicate the presence of C=C (284.6 eV), C-N (285.9 eV) and O-C=O (288.8 eV) bonding in prepared samples.[6] As for CPOC@C-800, the Co-C bonding around 779.4/795.8 eV replaces the Co-N bonding in CPOC@C-700, and the N-Co bonding is missing in N 1s spectra, implying the overheating disrupts the bonding between Co and N atoms.[7] The appearance of P-Co, O-Co and C-Co bonds in P 2p, O 1s and C 1s spectra, respectively, also indicates the partial decomposition of $Co_2P_2O_7$.[8]

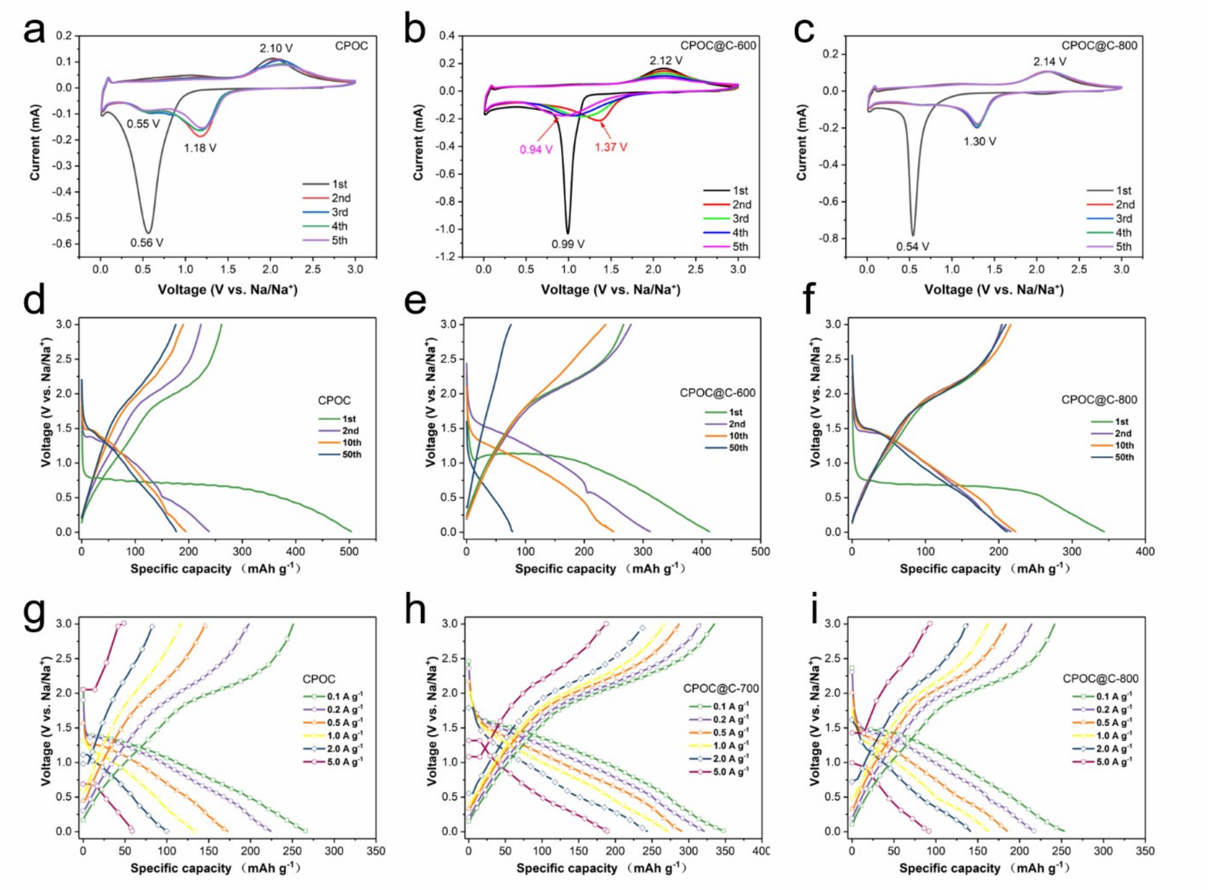

Fig. S7. The initial five successive CV curves of a) CPOC, b) CPOC@C-600 and c) CPOC@C-800. The discharge-charge curves at 100 mA g^{-1} and different current densities corresponding to rate capability of d, g) CPOC, e, h) CPOC@C-600 and f, i) CPOC@C-800.

Unlike the discharge profiles after the first cycle of CPOC@C-700, the second and tenth discharge curves of CPOC are divided into two regions by pits of about 0.5 V (Fig. S7d). These two regions correspond to the peaks of CV curves at 1.18 and 0.55 V (Fig. S7a). This seemingly have something to do with crystallinity and outer carbon layer. In fact, the improved reaction kinetics of CPOC@C-700 brought about by hierarchical conductive structure avoids the appearance of the pit. On the other hand, CPOC@C-600 maintains a discharge specific capacity of 200 mAh g^{-1} above the pit voltage from 1st to 10th cycle, but the specific capacity below the pit voltage decreases from 110 to 30 mAh g^{-1}. This implies that low crystallinity weakens the reversibility of Equation (2). CPOC@C-800 with higher crystallinity shows an enhanced platform at 1.5 V and low pit voltage (0.3 V). The discharge specific capacity below the pit voltage in the first cycle is only 40 mAh g^{-1}, far less than CPOC and CPOC@C-600, and keep almost unchanged from 1st to 100th cycle. This can be attribute to the fact that oversized grains reduce the utilization of $Co_2P_2O_7$ and overheating induced partial decomposition of $Co_2P_2O_7$.

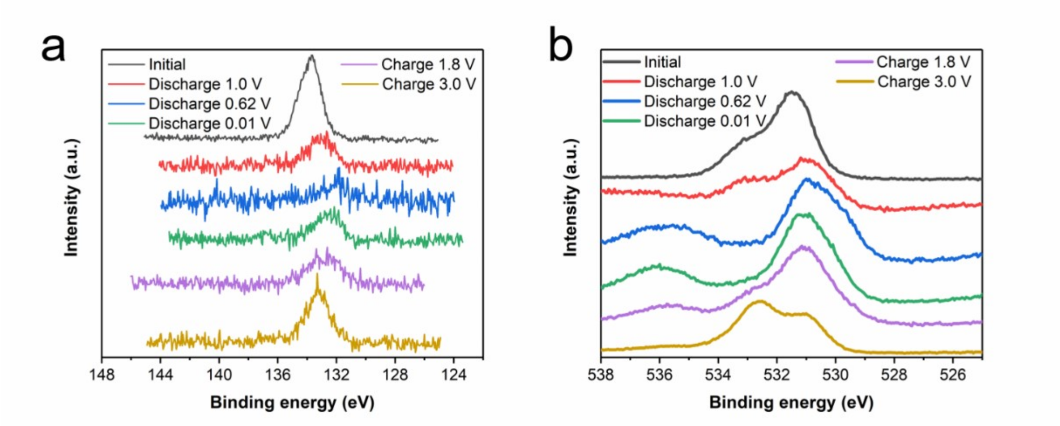

Fig. S8. The high-resolution spectra of a) P 2p and b) O 1s at different discharge/charge states.

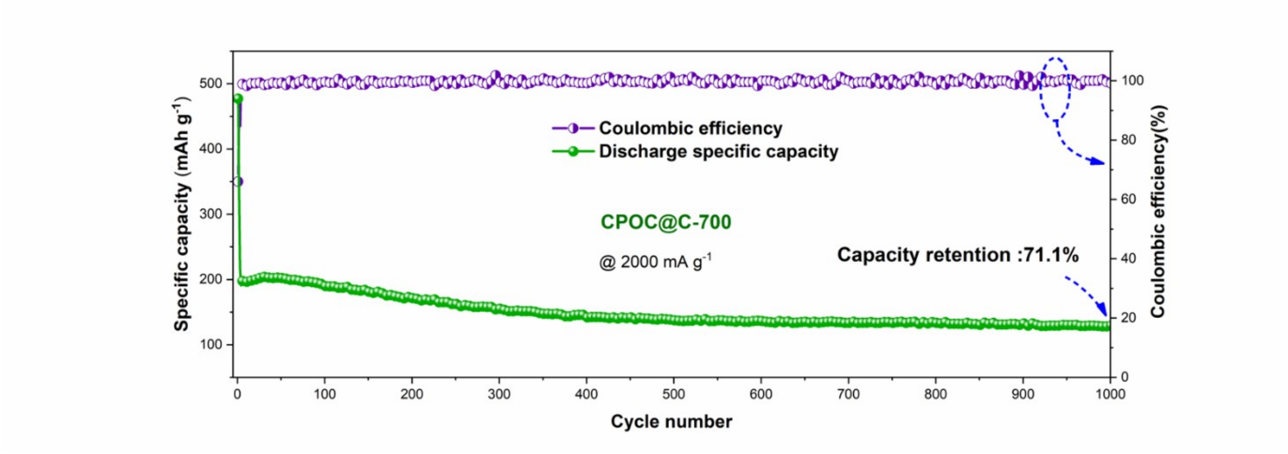

Fig. S9. Long cycling performance and coulombic efficiency of CPOC@C-700 at 2A g^{-1}.

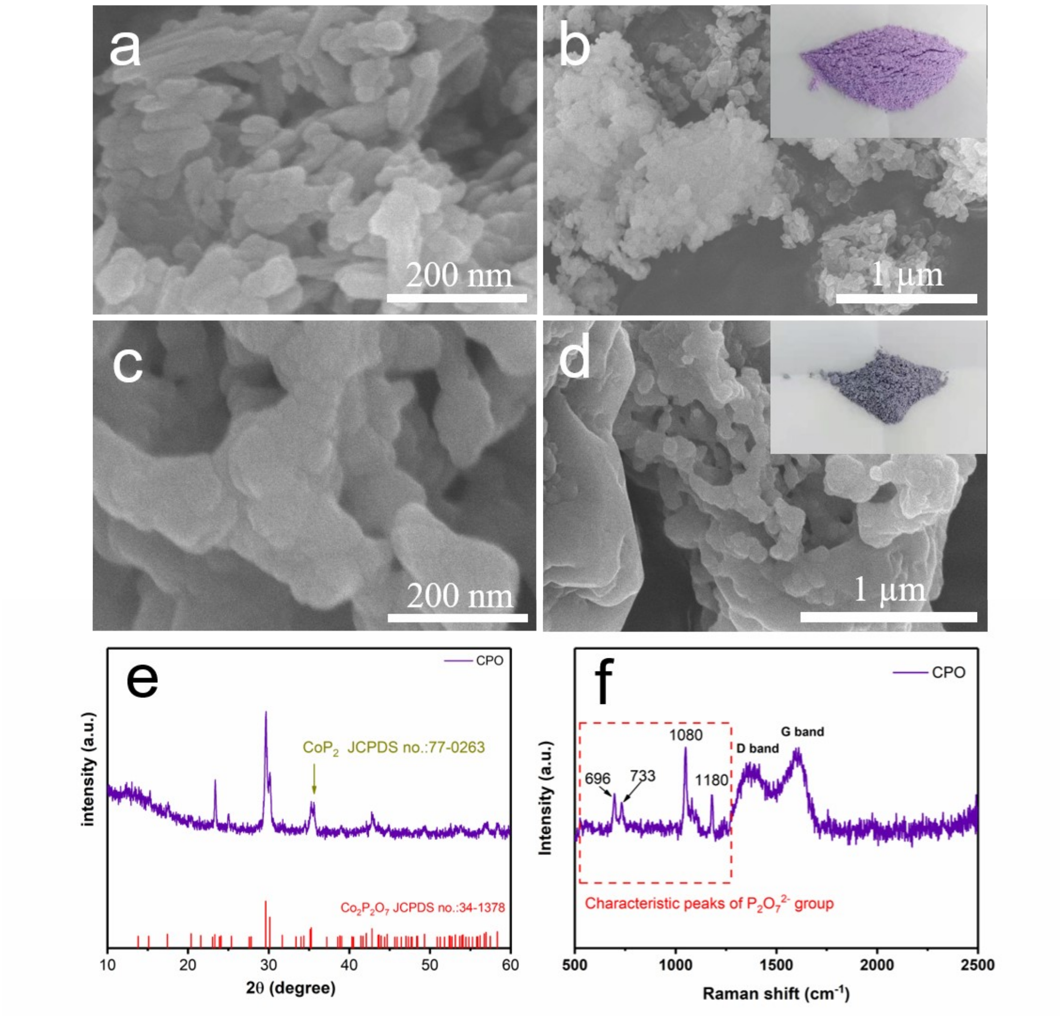

Fig. S10. The SEM images of a, b) precursor prepared from inorganic pyrophosphate (insets are the corresponding digital photos) and c, d) CPO. e) XRD pattern and f) Raman spectrum of CPO.

As shown in Fig. S10b and d, the light purple precursor prepared from $Na_2H_2P_2O_7$ and $Co(OOCCH_3)_2$ turned into grey purple after annealing at 700 °C for 2 hours. The XRD pattern of CPO in Fig. S9e shows the same phase as CPOC@C-700, except for the peak at 35.6°ascribed to CoP_2. This indicates the thermal stability of CPO is inferior to CPOC@C-700. The Raman spectrum exhibits two characteristic peaks of carbon derived from CH_3COO^- and four peaks attributed to the vibration of $P_2O_7^{2-}$.[9] The detectable of $P_2O_7^{2-}$ in Raman spectrum suggests the low carbon content in CPO.

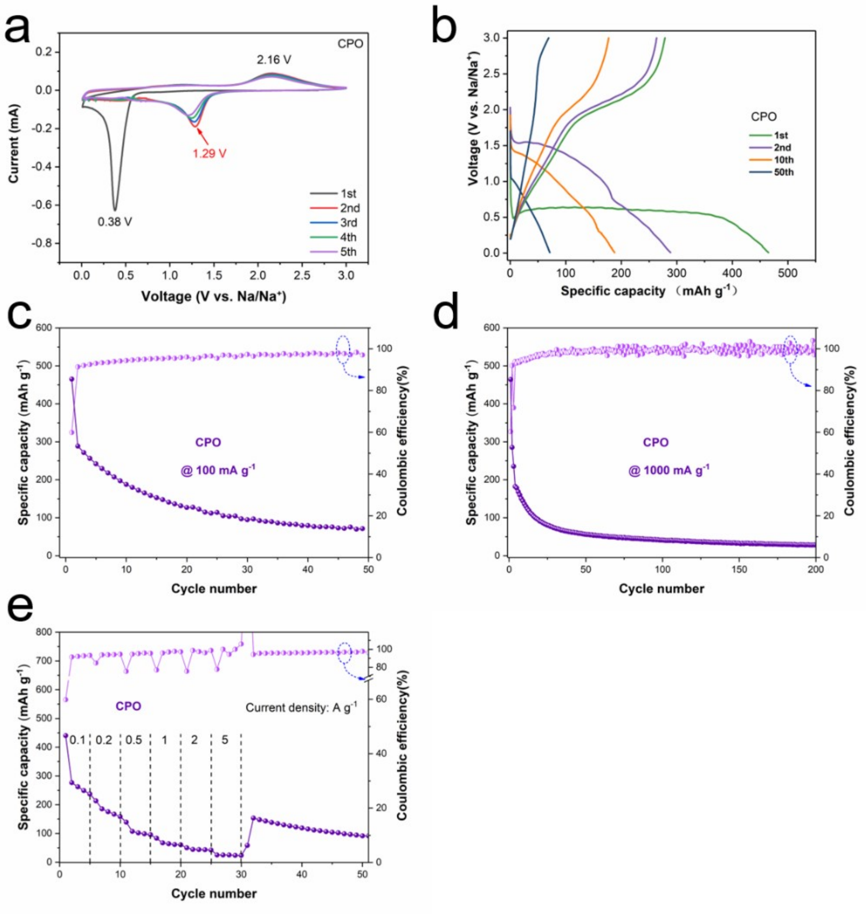

Fig. S11. The electrochemical characterizations of CPO. a) Initial five CV curves at 0.1 mV s^{-1}. b) The first, second, tenth and fiftieth discharge-charge profiles at a current density of 100 mA g^{-1}. The cycling performance at c) 100 mA g^{-1} and d) 1000 mA g^{-1}. e) Rate performance.

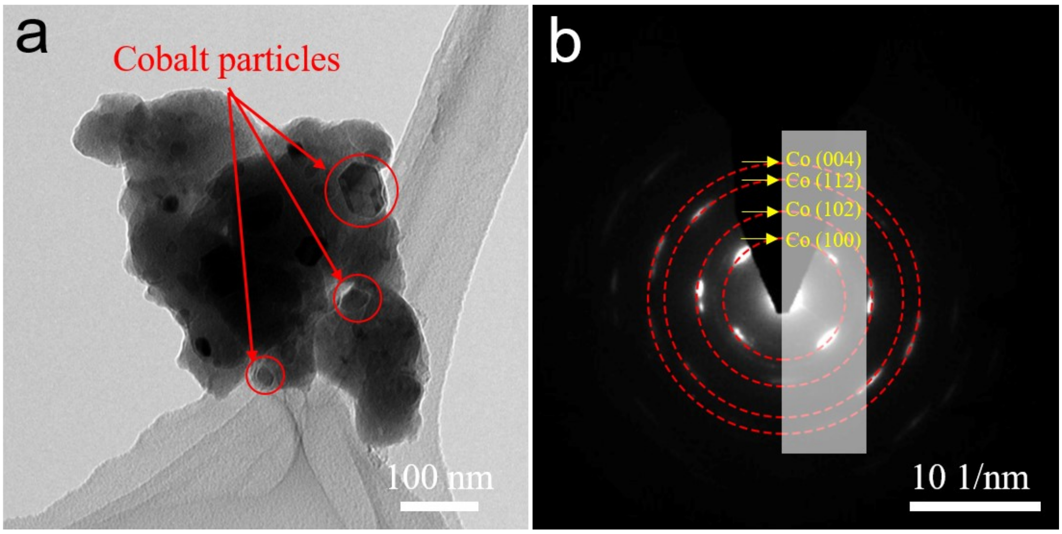

Fig. S12. a) TEM and b) SAED images of CPOC when discharge to 0.01 V.

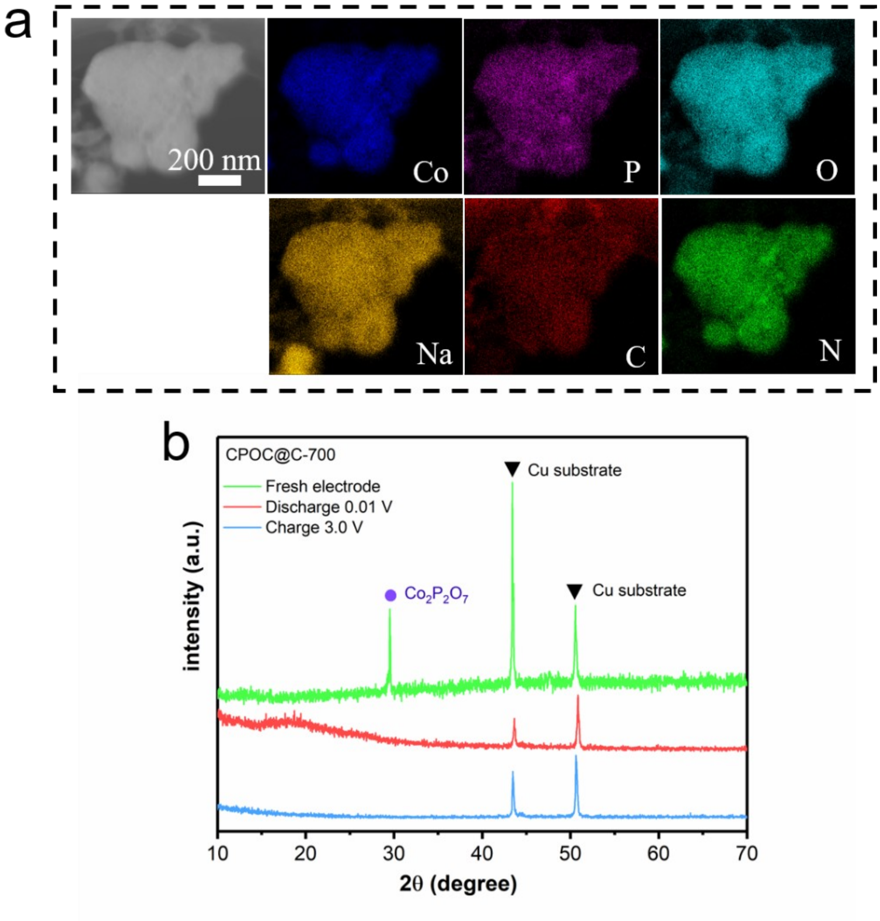

Fig. S13. a) Elemental mapping (C, N, Co, P, O, Na) images of CPOC@C-700 when discharge to 0.01 V. b) *Ex-situ* XRD of CPOC@C-700 electrode when discharge to 0.01 V and charge to 3.0 V.

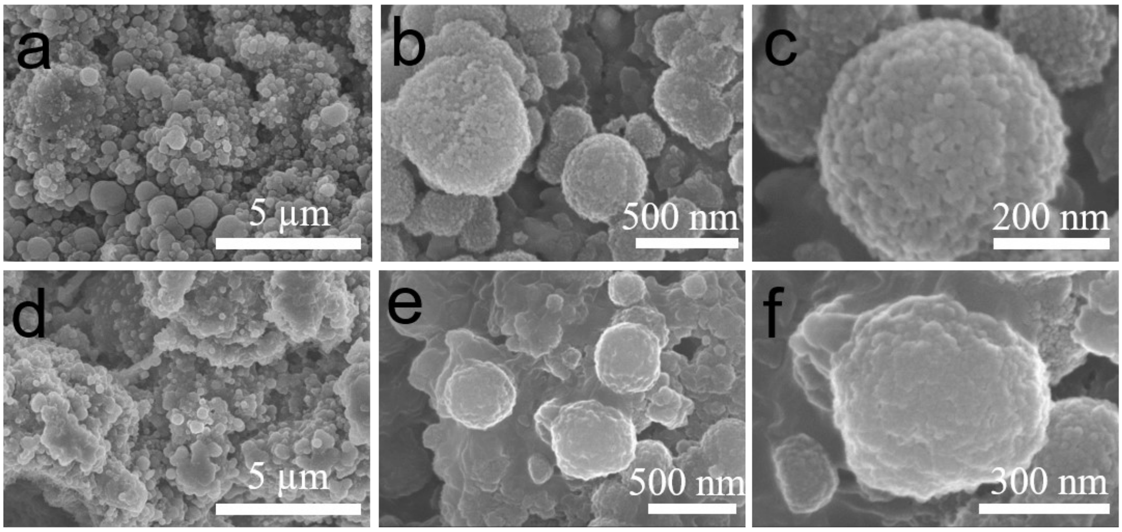

Fig. S14. *Ex-situ* SEM images of CPOC@C-700 at different magnifications after a, b, c) 1 cycle and d, e, f) 200 cycles at 100 mA g^{-1}.

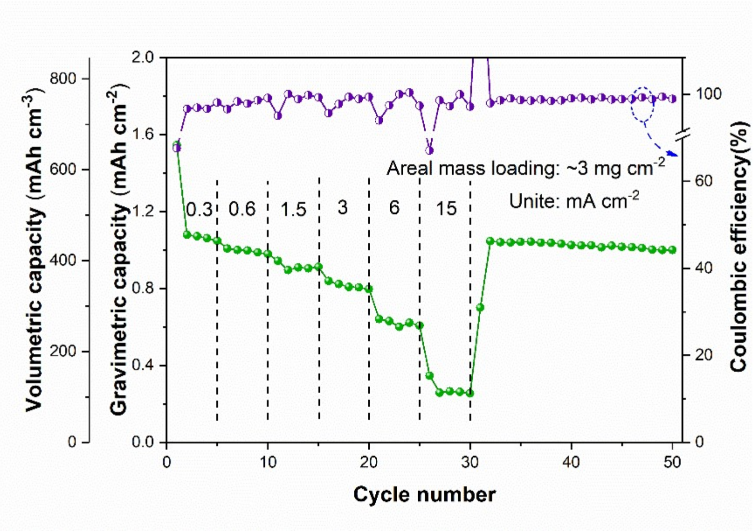

Fig. S15. The volumetric and gravimetric capacity of CPOC@C-700 at various rates.

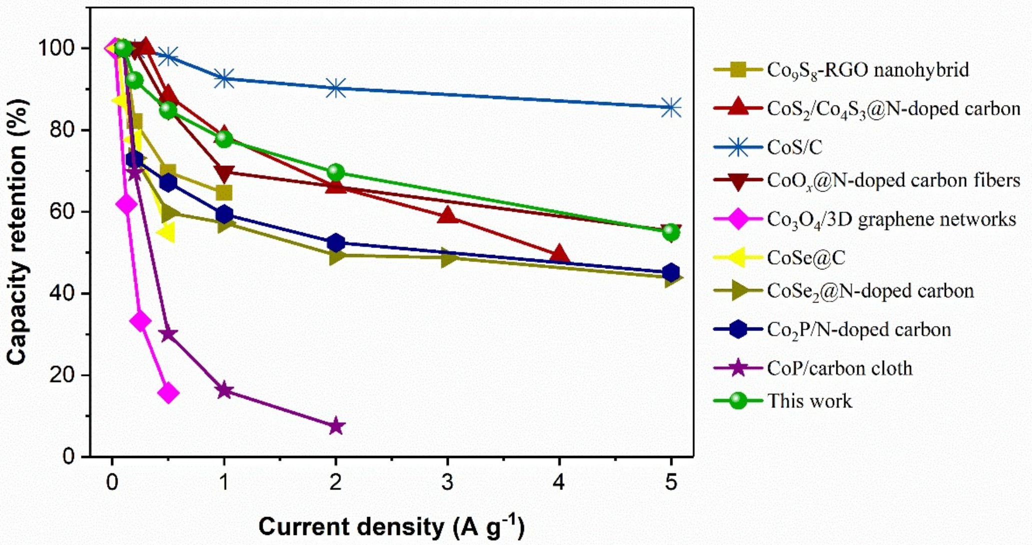

Fig. S16. Comparison of rate performance with reported cobalt-based anodes for SIBs.

Table S2. Comparison of cycling stability with reported cobalt-based anodes for SIBs.

Electrode materials$^{Ref.}$	**Current density**	**Cycle number**	**Capacity retention**	**Fading rate per cycle**
Co_9S_8-RGO nanohybrid[10]	0.1 A g^{-1}	30	81.2%	0.63%
CoS_2/Co_4S_3@N-doped carbon[11]	2 A g^{-1}	400	58.4%	0.10%
CoS/C[12]	1 A g^{-1}	2000	90.3%	0.0048%
CoO_x@N-doped carbon fibers[13]	2 A g^{-1}	6000	92.2%	0.0013%
Co_3O_4/3D graphene networks[14]	0.025 A g^{-1}	50	95.2%	0.10%
CoSe@C[15]	0.1 A g^{-1}	60	69.3%	0.51%
$CoSe_2$@N-doped carbon[16]	1 A g^{-1}	500	56.4%	0.087%
Co_2P/N-doped carbon[17]	1 A g^{-1}	2500	57.5%	0.017%
CoP/carbon cloth[18]	1 A g^{-1}	2000	86.4%	0.0068%
This work	2 A g^{-1}	1000	71.1	0.029%

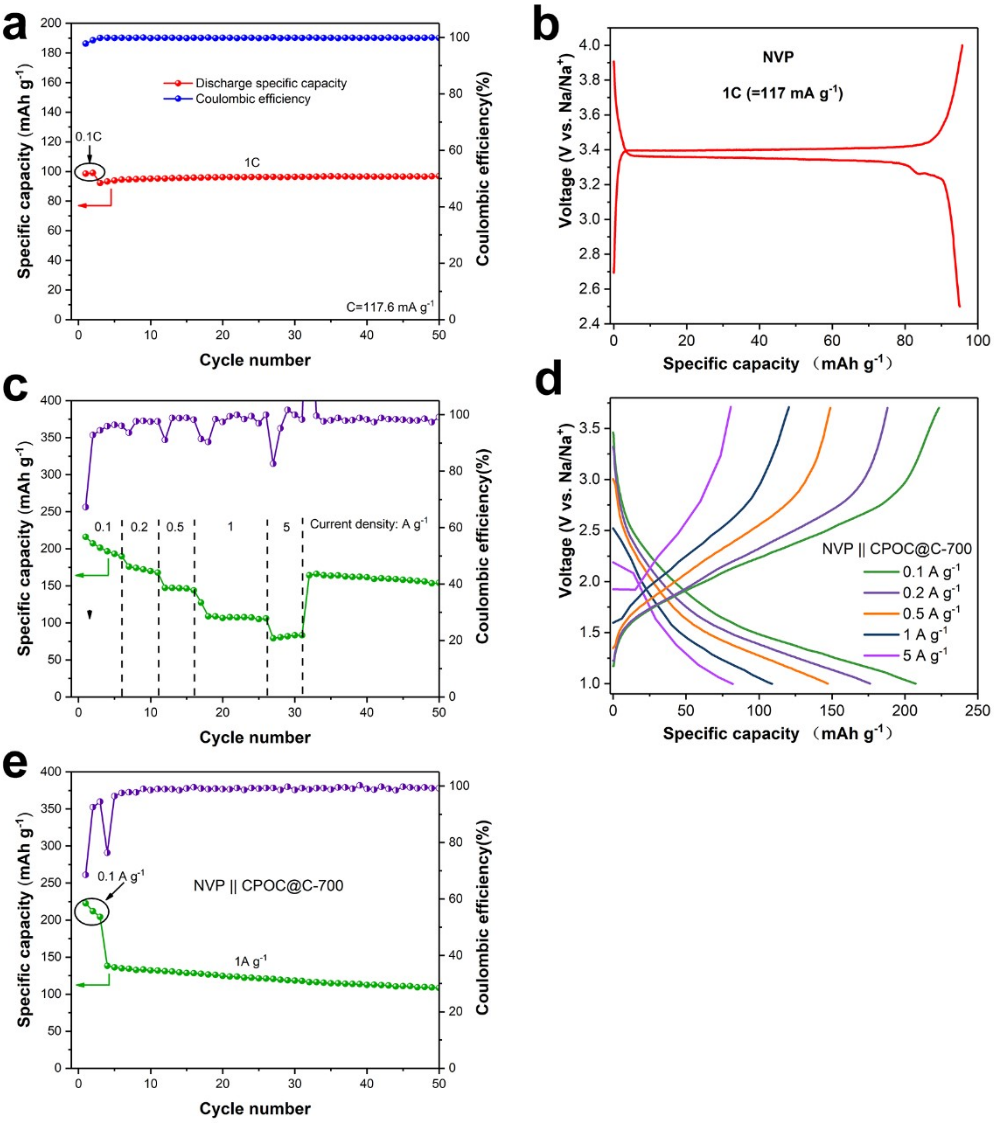

Fig. S17. The electrochemical characterizations of a, b) NVP half cells and c, d, e)NVP||CPOC@C-700 full batteries. a, e) Cycling stability test, b, d) discharge-charge curves, and c) rate performance.

According to the reports of Dun Bruce and Simon Peter et.al, there is a power-law relationship between the measured current (i) and sweep rates (v) of CV curves:[19]

$$i = \mathrm{a}v^{\mathrm{b}} \qquad \text{Equation (S1)}$$

where the b values can be obtained by fitting the slop of log(v)-log(i) plots.

The diffusive contribution and capacitive contribution can be quantified by Equations (S2) or (S3):

$$i(\mathrm{V}) = k_1 v + k_2 v^{1/2} \qquad \text{Equation (S2)}$$

or

$$i/v^{1/2} = k_1 v^{1/2} + k_2 \qquad \text{Equation (S3)}$$

Both k_1 and k_2 are constants at a given potential.

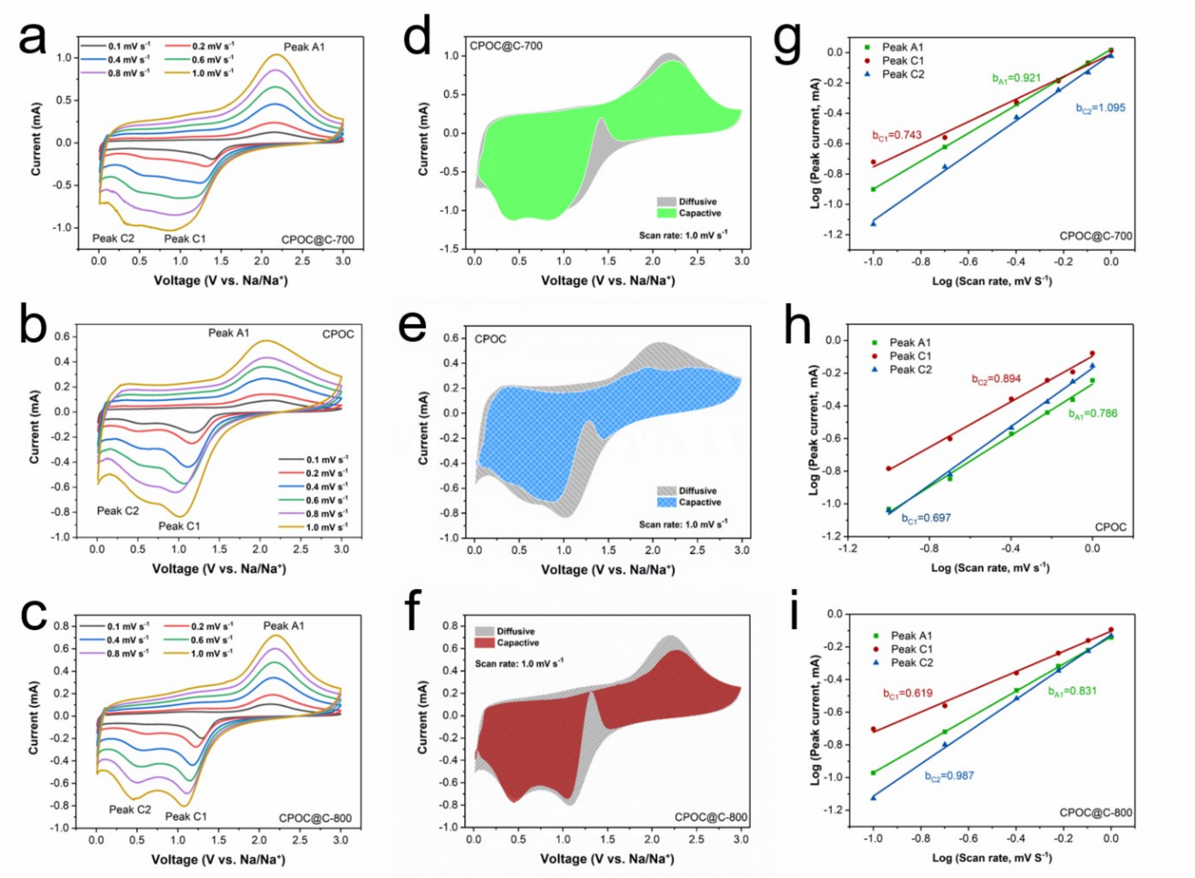

Fig. S18. CV curves of a)CPOC@C-700, b) CPOC and c) CPOC@C-800 at different scan rates from 0.1 to 1.0 mV s^{-1}. Typical voltage profile of d) CPOC@C-700, e) CPOC and f) CPOC@C-800 for calculated capacitive current and measured current at 1 mV s^{-1}. Log (i) versus log (v) plots at specific peak currents of g)CPOC@C-700, h) CPOC and i) CPOC-800.

Table S3. The b values of peak current of CPOC@C-700, CPOC@C-800 and CPOC.

Samples	**A1**	**C1**	**C2**
CPOC@C-700	0.921	0.743	1.095
CPOC@C-800	0.831	0.619	0.987
CPOC	0.786	0.697	0.894

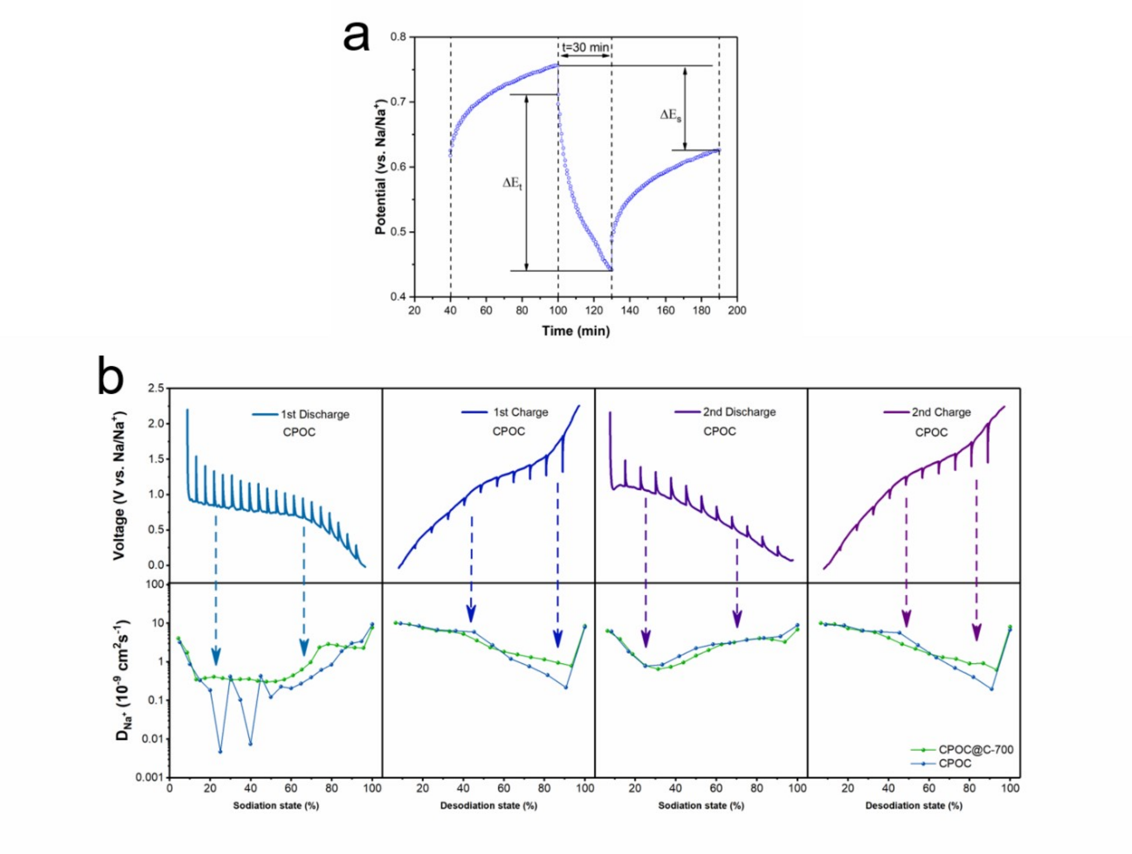

Fig. S19. a) E vs. t curves of CPOC@C-700 electrode for a single discharge impulse. b) GITT curves and corresponding Na^+ diffusion coefficient at different sodiation/desodiation states of the CPOC and CPOC@C-700 electrodes.

The sodium-ion diffusion coefficient was measured by GITT and calculated by Equation S4 as follows:[20]

$$D = \frac{4L^2}{\pi\tau}\left(\frac{\Delta E_s}{\Delta E_\tau}\right)^2 \qquad \text{Equation (S4)}$$

Where t is the duration of the imposed current pulse (s), τ represents the relaxation time (s), and ΔE_s means the steady-state potential change (V) caused by the imposed current pulse. ΔE_t is the potential change (V) during the constant current pulse after eliminating the iR drop. L is sodium-ion diffusion distance (cm); here is approximately equal to the thickness of the electrode material.

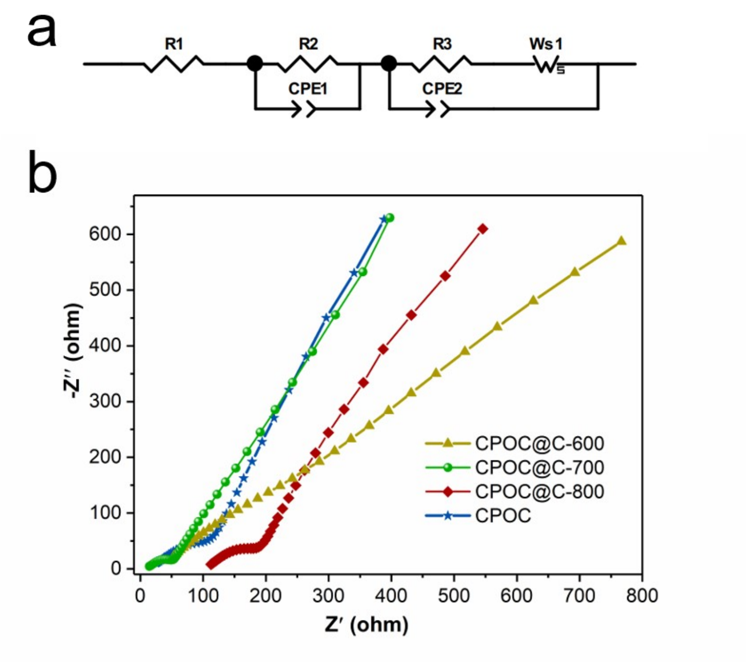

Fig. S20. a) Fitting equivalent circuit and b) the Nyquist plots of CPOC and CPOC@Cs after 5 discharge-charge cycles.

Table S4. The EIS fitting parameters of CPOC@C-700, CPOC@C-800 and CPOC.

Samples	**R_1**	**R_2**	**R_3**
CPOC@C-700	11.55	61.71	10.29
CPOC@C-800	109.8	83.74	313.5
CPOC	17.88	111.3	510.4

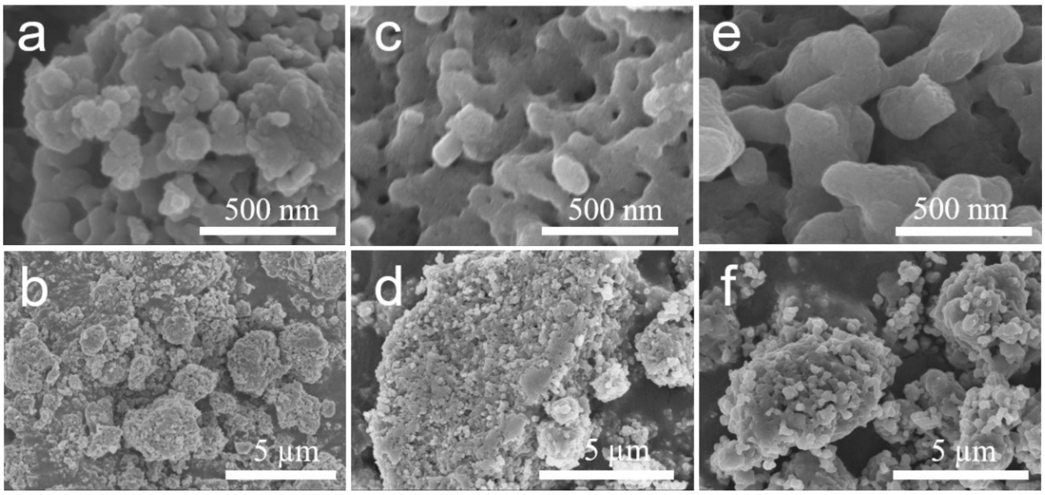

Fig. S21. SEM images of a, b) MPOC@C-600, c, d) FPOC@C-700 and e, f) ZPOC@C-700 at different magnifications.

References

1. L. R. Hou, L. Lian, D. K. Li, J. D. Lin, G. Pan, L. H. Zhang, X. G. Zhang, Q. G. Zhang and C. Z. Yuan, *RSC Adv.*, 2013, **3**, 21558-21562.
2. X. X. Cao, A. Q. Pan, S. N. Liu, J. Zhou, S. T. Li, G. Z. Cao, J. Liu and S. Q. Liang, *Adv. Energy Mater.*, 2017, **7**, 1700797.
3. A. Dehghani, F. Poshtiban, G. Bahlakeh and B. Ramezanzadeh, *Constr. Build. Mater.*, 2020, **239**, 117812.
4. F. F. Li, Z. H. He, J. F. Gao and L. B. Kong, *Ionics*, 2020, **26**, 2989-3001.
5. A. Padhy, A. K. Samantara and J. N. Behera, *Sustainable Energy Fuels*, 2021, **5**, 3729-3736.
6. F. Zhang, E. Alhajji, Y. J. Lei, N. Kurra and H. N. Alshareef, *Adv. Energy Mater.*, 2018, **8**, 1800353.
7. Q. Guo, S. G. Xia, X. B. Li, Y. Wang, F. Liang, Z. S. Lin, C. H. Tung and L. Z. Wu, *Chem. Commun.*, 2020, **56**, 7849-7852.
8. Q. N. Liu, Z. Hu, Y. R. Liang, L. Li, C. Zou, H. L. Jin, S. Wang, H. M. Lu, Q. F. Gu, S. L. Chou, Y. Liu and S. X. Dou, *Angew. Chem. Int. Ed.*, 2020, **59**, 5159-5164; *Angew. Chem.*, 2020, **132**, 5197-5202.
9. B. Boonchom and R. Baitahe, *Mater. Lett.*, 2009, **63**, 2218-2220.
10. G. H. Zhan, Z. D. Lin, B. Xu, B. Yang, X. Chen, X. L. Wang, C. S. Yang and J. Q. Liu, *J. Mater. Sci.: Mater. Electron.*, 2017, **28**, 13710-13715.
11. C. F. Dong, L. J. Guo, H. B. Li, B. Zhang, X. Gao, F. Tian, Y. T. Qian, D. B. Wang and L. Q. Xu, *Energy Storage Mater.*, 2020, **25**, 679-686.
12. L. M. Zhou, K. Zhang, J. Z. Sheng, Q. Y. An, Z. L. Tao, Y. M. Kang, J. Chen and L. Q. Mai,

Nano Energy, 2017, **35**, 281-289.

13. C. Yang, Y. Z. Li, B. B. Zhang, Y. B. Lian, Y. Ma, X. H. Zhao, X. Q. Zeng, J. S. Li, Z. Deng, J. Ye, W. B. Wu and Y. Peng, *Nanoscale*, 2020, **12**, 8922-8933.
14. Y. G. Liu, Z. Y. Cheng, H. Y. Sun, H. Arandiyan, J. P. Li and M. Ahmad, *J. Power Sources*, 2015, **273**, 878-884.
15. M. Y. Wang, H. N. Guo, C. H. An, Y. Zhang, W. Q. Li, Z. T. Zhang, G. S. Liu, Y. F. Liu and Y. J. Wang, *J. Alloy Compd.*, 2020, **820**, 153090.
16. F. J. Kong, J. Wang, J. Y. Chen, S. Tao, B. Qian and H. M. Luo, *Chem. Commun.*, 2020, **56**, 9218-9221.
17. X. F. Li, X. Q. Zhu, J. Li, P. Liu, M. Huang and B. Xiang, *J. Alloy Compd.*, 2020, **846**, 156256.
18. Z. G. Yang, Q. Pan, Z. G. Wu, W. Xiang, F. Y. Fu, Y. Wang, L. Ji, B. H. Zhong, X. P. Sun and X. D. Guo, *J. Alloy Compd.*, 2020, **848**, 156285.
19. J. Wang, J. Polleux, J. Lim and B. Dunn, *J. Phys. Chem.*, *C* 2007, **111**, 14925-14931.
20. G. Z. Fang, Z. X. Wu, J. Zhou, C. Y. Zhu, X. X. Cao, T. Q. Lin, Y. M. Chen, C. Wang, A. Q. Pan and S. Q. Liang, *Adv. Energy Mater.*, 2018, 8. 1703155.